MATERIALS CHEMISTRY
FRONTIERS

CHINESE CHEMICAL SOCIETY

ROYAL SOCIETY OF CHEMISTRY

RESEARCH ARTICLE

View Article Online
View Journal | View Issue

Cite this: *Mater. Chem. Front.*, 2022, **6**, 724

Designing a novel Eu^{2+}-doped hafnium-silicate phosphor for an energy-down-shift layer of $CsPbI_3$ solar cells

Yixin Li, Shichuan Wang and Yuhua Wang *

Received 25th December 2021,
Accepted 19th January 2022

DOI: 10.1039/d1qm01655e

rsc.li/frontiers-materials

The excessive carbon discharge and low utilization efficiency of solar energy are still the biggest challenges in the world. A series of Eu^{2+} doped K_2HfSiO_5 phosphors were synthesized and applied in $CsPbI_3$ perovskite solar cells. Under the excitation of ultraviolet and near ultraviolet light in the range of 300–450 nm, K_2HfSiO_5:Eu^{2+} exhibits emission in the visible range of 450–650 nm. Due to their strong absorption in the ultraviolet region and high quantum efficiency, K_2HfSiO_5:Eu^{2+} phosphors could be used to fabricate an energy-down-shift layer for solar cells. When spin-coated with the layer, the value of the short-circuit current of the packaged $CsPbI_3$ solar cell increased, resulting in the enhancement of the power conversion efficiency by 2.19%. In addition, other basic properties of K_2HfSiO_5:Eu^{2+} phosphors such as photoluminescence, cathodoluminescence and stability have also been studied. All the results indicate that the energy-down-shift layer made using K_2HfSiO_5:Eu^{2+} phosphors has a positive effect on improving the performance of $CsPbI_3$ perovskite solar cells.

1. Introduction

In recent years, a luminescence energy-down-shift (EDS) layer for solar cells has received much attention because of its obvious light conversion effect.[1–3] By converting the light that is useless for solar cells (ultraviolet (UV) or infrared (IR) light) into the useful visible or near infrared light, the EDS layers allow solar cells to produce more carriers, thus improving their power conversion efficiency (PCE).[4–6] Therefore, researching and developing EDS layers for solar cells are of great significance for the utilization of solar energy and clean energy.

Among several types of solar cells, $CsPbI_3$ perovskite solar cells have aroused interest due to their desirable band gap (about 1.73 eV), strong light absorption and outstanding photoelectric properties.[7–9] $CsPbI_3$ is considered to be one of the materials with the most potential as a new photovoltaic material for the next generation. According to some existing reports, inorganic quantum dots, carbon dots, up-conversion phosphors and metal clusters could serve as EDS layers for $CsPbI_3$ solar cells.[5,10–12] In these studies, although the performance of the solar cells has been enhanced to a certain extent, numerous shortcomings still exist. For example, the synthetic process of quantum dots is very complex, relating to many toxic raw materials which are harmful to human health and have a poor stability when set in an air environment. Besides, the photoluminescence quantum yield of most EDS layers made by up-conversion phosphors is very low, which affects the PCE of solar cells. Furthermore, though metal nano cluster luminescent materials have a high quantum efficiency, their fabrication cost is so high that they are not suitable for large-scale application. Hence, it is necessary for us to search for a novel light-conversion material which could be applied to the EDS layer for $CsPbI_3$ solar cells with low costs and convenience of preparation.

As is well known, the range of the solar spectrum is from UV to IR light. However, the $CsPbI_3$ solar cells cannot effectively utilize UV light because the photoelectric reaction in this region is weak. Instead, it has a strong photoelectric effect in the visible range (400–800 nm).[13,14] As a type of light conversion material, phosphors have many advantages such as suitable size, excellent luminous efficiency, preferable stability, intense absorption in the UV region and low energy consumption.[15–18] Consequently, phosphors with a down-conversion (DC) effect could better satisfy with the requirements of the EDS layer for $CsPbI_3$ solar cells.[19]

It is worth mentioning that Eu^{2+} doped phosphors generally exhibit a broad-band emission according to the 4f–5d transition, so that they have outstanding luminescence features.[20] Most part of Eu^{2+} activated phosphors which can be used in the EDS layer are nitrides such as $CaAlSiN_3$:Eu^{2+}, $SrSi_2O_2N_2$:Eu^{2+}

Department of Materials Science, School of Materials and Energy, Key Laboratory of Special Function Materials and Structure Design of Ministry of Education, National and Local Joint Engineering Laboratory for Optical Conversion Materials and Technology of National Development and Reform Commission, Lanzhou University, Lanzhou 730000, P. R. China. E-mail: wyh@lzu.edu.cn

and $(Ca,Sr)_2Si_5N_8$:Eu^{2+}, Tm^{3+}; they all have a favourable luminescence performance.[21–23] However, it is very hard to synthesize nitrides because of their rigorous preparation conditions (high temperature and high pressure) and because the cost of their fabrication process is tremendously high. Silicate based phosphors are a superior choice; many of them have tremendous potential for photoluminescence and cathodoluminescence materials such as $NaScSi_2O_6$:Eu^{2+}, $RbNa_3(Li_3SiO_4)_4$:Eu^{2+} and Sr_3SiO_5:Eu^{2+} because of their luminescence properties, splendid chemical and physical stability and so on.[24–26] Thus, when combining with polyvinyl pyrrolidone (PVP), the luminescence performance of the silicate phosphor will not be influenced due to its great stability. In addition, silicates are easily available and low cost, widely used in basic research studies.[27–29] In this work, we had prepared a K_2HfSiO_5:Eu^{2+} phosphor *via* replacing Zr in K_2ZrSiO_5:Eu^{2+} with Hf through the solid-state reaction. The highest internal quantum efficiency was nearly about 60% and the thermal stability was greatly improved.[30] Then the K_2HfSiO_5:Eu^{2+} phosphor was successfully applied onto the $CsPbI_3$ perovskite solar cells as an EDS layer. It is found that both short-circuit current (J_{sc}) and PCE are distinctly increasing. Meanwhile, the cathodoluminescence properties of the K_2HfSiO_5:Eu^{2+} phosphor were also explored, demonstrating that it has the potential for multifunctional application.

2. Experimental

Phosphor preparation

The K_2HfSiO_5:Eu^{2+} phosphor was fabricated through the high temperature solid-state method. The initial raw materials were K_2CO_3 (A.R), HfO_2 ($\geq$99.9%), SiO_2 (A.R.) and Eu_2O_3 (99.99%). They were mixed together in a stoichiometric ratio, and 3 wt% H_3BO_3 was used as the flux. The mixture was ground homogeneously with alcohol for 20 minutes and then put into several alumina crucibles. The heating rate was set to 3 °C min^{-1}. After calcination in a tube furnace at 1120 °C for 6 h in a reduced atmosphere ($H_2:N_2 = 5:95$), the products were taken out and cooled down to room temperature and ground again for further analysis.

EDS layer fabrication

The crude materials of the EDS layer were K_2HfSiO_5:$0.02Eu^{2+}$ phosphor, PVP and ethanol. They were weighed according to the mass ratio of 1 : 10 : 50, and then PVP and ethanol were added into a beaker for stirring. After PVP dissolves, the K_2HfSiO_5:$0.02Eu^{2+}$ phosphor was added into the beaker and stirring was continued for another 30 minutes. Finally, the EDS layer solution in the middle of the beaker was spin-coated on the near light side of the $CsPbI_3$ solar cells in a glove box at 2000 rpm for 30 s at room temperature.

Device fabrication

Precursor solution preparation: all experiments were carried out in a glove box that was filled with N_2. CsI and PbI_2 were weighed according to the stoichiometric ratio in the container, 0166 g DAMI and 1 ml DMF were weighed, respectively; DMF-d7 was added according to the volume ratio of 5%, and magnetic stirring was carried out for more than 6 h.

Packaged solar cell preparation: the precursor solution was spin coated on the TiO_2/FTO surface which was treated with peroxide plasma for 35 s at 3000 rpm. Then it was annealed at 210 °C for 10 min to obtain the $CsPbI_3$ film. After this, the device was assembled as an EDS layer/FTO/TiO_2/$CsPbI_3$ film/spiro-OMeTAD/electrode structure, and finally the spin coated $CsPbI_3$ device was obtained.

Measurements and characterization

The phase of the instrument of X-ray powder diffraction (XRD) was Bruker D2 PHASER X-ray diffractometer with Cu Kα radiation. The range of the measured 2θ was 10–80°, the set step length was 0.03° and the counting time was 0.1 s per step. The XRD Rietveld refinement result of the K_2HfSiO_5 host was obtained using the General Structure Analysis System (GSAS).[31] Both the morphology and Energy Dispersive X-Ray (EDX) spectra were obtained using a scanning electron microscope (SEM) and a transmission electron microscope (TEM). Density functional theory (DFT) was used to calculate the band structure with the help of the Cambridge Serial Total Energy Packet (CASTEP) code.[32] The diffuse reflectance spectra (DRS) were obtained using an UV-vis spectrophotometer (PE-Lambda 950) and $BaSiO_4$ powders were used as a reference. The photoluminescence (PL) and photoluminescence excitation (PLE) spectra and decay curves were detected using a FLS-920T fluorescence spectrophotometer. At the same time, thermal stability was tested with the same PL equipment and a TAP-02 heating device was added. The cathodoluminescence (CL) properties of K_2HfSiO_5:Eu^{2+} phosphors were measured using a Mp-Micro-S instrument. The current density–voltage (I–V) curves were recorded *via* the illumination of an AM 1.5G (100 mW cm^{-2}) solar simulator (Enlitech). The external quantum efficiency (EQE) spectra were measured using a Quantum efficiency tester (QE-R, Enlitech).

3. Results and discussion

Crystal structure and phase information

The XRD Rietveld refinement was introduced to acquire the detailed crystal structure of K_2HfSiO_5. For the sake of acquiring the phase information, K_2ZrSiO_5 was set as an initial model. The refinement results are shown in Fig. 1(a). The calculated data agree well with the experimental data and the refined factors are $R_{wp} = 8.52\%$, $R_p = 7.67\%$ and $\chi^2 = 1.31$, respectively. These parameters illustrated that the results of refinement have a referential value. The total refinement crystal data are shown in Table 1. It could be known that K_2HfSiO_5 is a monoclinic crystal system and its space group belongs to $p121/c1(14)$, and the atom coordinates are listed in Table 2.

According to the XRD patterns of K_2HfSiO_5:xEu^{2+} ($0 \leq x \leq 0.35$) samples shown in Fig. 1(b), with the increasing amounts

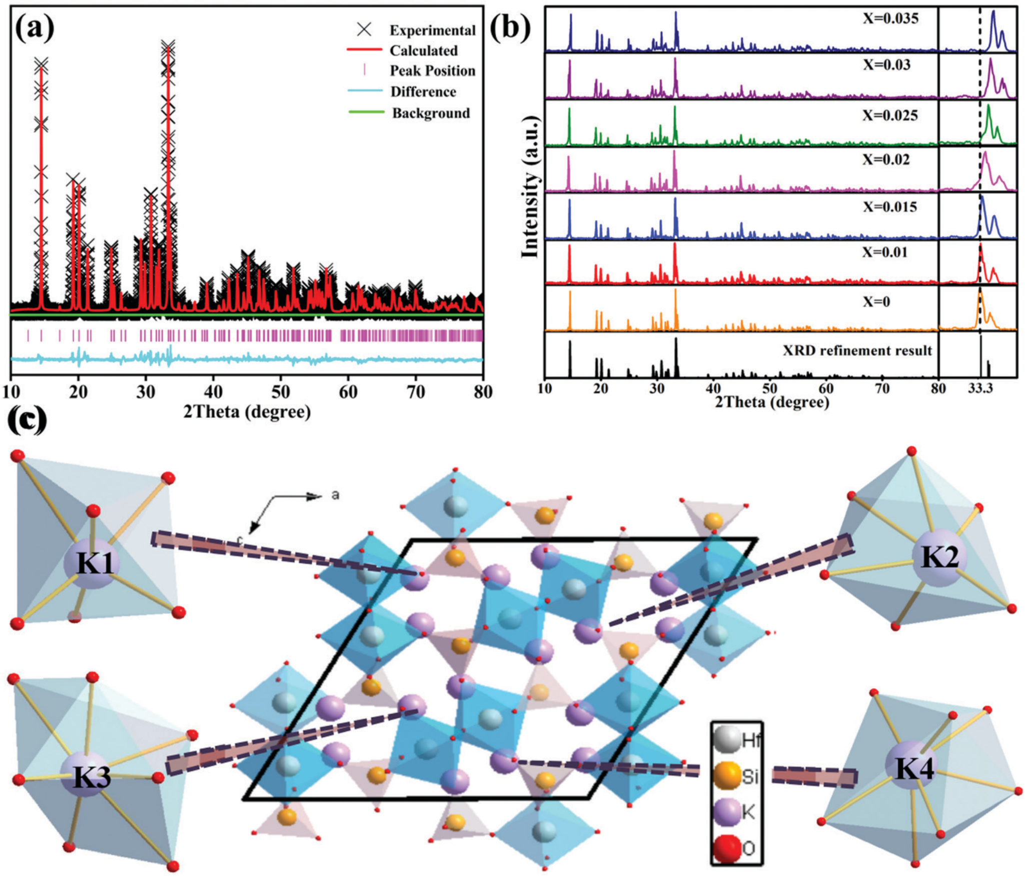

Fig. 1 (a) The K_2HfSiO_5 host Rietveld refinement result; (b) XRD patterns of K_2HfSiO_5:$x$$Eu^{2+}$ ($0.00 \leq x \leq 0.035$); and (c) the crystal structure sketch map of K_2HfSiO_5 and the different coordination surroundings of K^+.

Table 1 Crystal data of K_2HfSiO_5

Formula	K_2HfSiO_5
Crystal system	Monoclinic
Z	8
V	975.51(32) $Å^3$
Space-group	$P121/c1$ (14)
P	4.97 g cm^{-3}
A	14.10(18) Å
B	5.67 Å
C	14.09 Å
A	90.00°
B	90.00°
Γ	119.98°
χ^2	1.311
R_{wp}	8.52%
R_p	7.67%

Table 2 Atomic coordinates of K_2HfSiO_5

Atom	Wyckoff	x/a	y/b	z/c
K1	4e	0.291(5)	0.778(6)	0.144(8)
K2	4e	0.075(3)	0.752(6)	0.126(4)
K3	4e	0.195(6)	0.221(2)	0.332(6)
K4	4e	0.430(6)	0.250(3)	0.071(7)
Hf1	4e	0.065(8)	0.739(3)	0.369(2)
Hf2	4e	0.434(2)	0.235(8)	0.309(4)
Si1	4e	0.161(3)	0.244(9)	0.088(6)
Si2	4e	0.338(4)	0.761(2)	0.394(6)
O1	4e	0.127(8)	0.102(4)	0.461(5)
O2	4e	0.289(9)	0.254(3)	0.150(9)
O3	4e	0.408(9)	0.789(13)	0.041(8)
O4	4e	0.212(9)	0.714(7)	0.362(5)
O5	4e	0.092(14)	0.303(9)	0.129(7)
O6	4e	0.378(9)	0.596(22)	0.338(15)
O7	4e	0.134(2)	0.934(7)	0.027(3)
O8	4e	0.363(1)	0.064(8)	0.392(6)
O9	4e	0.007(12)	0.474(4)	0.272(8)
O10	4e	0.492(10)	0.966(3)	0.263(1)

of the introduced Eu ions, all the diffraction peaks are in accordance with the refinement result. The Eu^{2+} ions are considered to occupy the position of K^+ because the values of the ionic radii of Eu^{2+} (1.17 Å, coordination number (CN) = 6; 1.2 Å, CN = 7) are close to those of K^+ (1.38 Å, CN = 6; 1.46 Å, CN = 7), and much higher than those of Hf^{4+} (0.71 Å, CN = 6; 0.76 Å, CN = 7). It is worth noting in the partial enlarged patterns that the position of the diffraction peak at 33.3° gradually shifts to larger 2θ with Eu^{2+} doping. This phenomenon could be attributed to the fact that smaller radius (Eu^{2+}) ions occupy the site of the larger ions (K^+). According to the Bragg formula, when the smaller ions substituted the larger ones, the crystal lattice would shrink, leading to an increase of θ.[33]

Table 3 Average bond lengths (Å)

Bond	Distance
K1–O(CN = 6)	2.658(6)
K2–O(CN = 6)	2.587(3)
K3–O(CN = 7)	2.714(9)
K4–O(CN = 7)	2.663(2)

All the above results indicate that Eu ions are successfully doped into the K_2HfSiO_5 host and there is no impurity phase.

Fig. 1(c) displays the structure of K_2HfSiO_5. One $[SiO_4]^{4-}$ tetrahedron is connected with another $[HfO_6]^{8-}$ octahedron by sharing one O^{2-}, and one $[Hf_2O_{11}]^{14-}$ unit also consisted of two $[HfO_6]^{8-}$ octahedra. A variety of polyhedron pairs constituting a 3D framework of K_2HfSiO_5 and the isolated K^+ act as cations which could be substituted by doped ions. There are four different coordination surroundings of K^+ (K1, CN = 6; K2, CN = 6; K3, CN = 7 and K4, CN = 7) and as listed in Table 3, the average bond lengths of K1–O, K2–O, K3–O and K4–O are 2.658 Å, 2.587 Å, 2.714 Å and 2.663 Å, respectively.

Fig. 2(a) reveals the SEM image of K_2HfSiO_5:$0.02Eu^{2+}$ particles. The shape of the sample is irregular rod distribution, the ranges of the length and diameter are 10–15 μm and 2–5 μm, respectively. The SEM mapping image of the sample is shown in Fig. 2(b). It could be seen from the image that K, Hf, Si, O and Eu elements are detected and uniformly distributed on the selected particle surface. In addition, TEM and the High-Resolution Transmission Electron Microscope (HRTEM) graphs of K_2HfSiO_5:$0.02Eu^{2+}$ are shown in Fig. 2(c). The stable crystal lattice could be seen clearly and the distance between two adjacent crystal planes is 0.4515 nm, which corresponds to the (111) crystal plane. The different element compositions of K_2HfSiO_5:$0.02Eu^{2+}$ are exhibited in Fig. 2(d). There are no other elements in the sample (the C peak is attributed to the instrument) and it could be observed from the insight table that the stoichiometric ratio of each element has exactly constituted K_2HfSiO_5. These characterization methods demonstrated the successful preparation of K_2HfSiO_5:Eu.

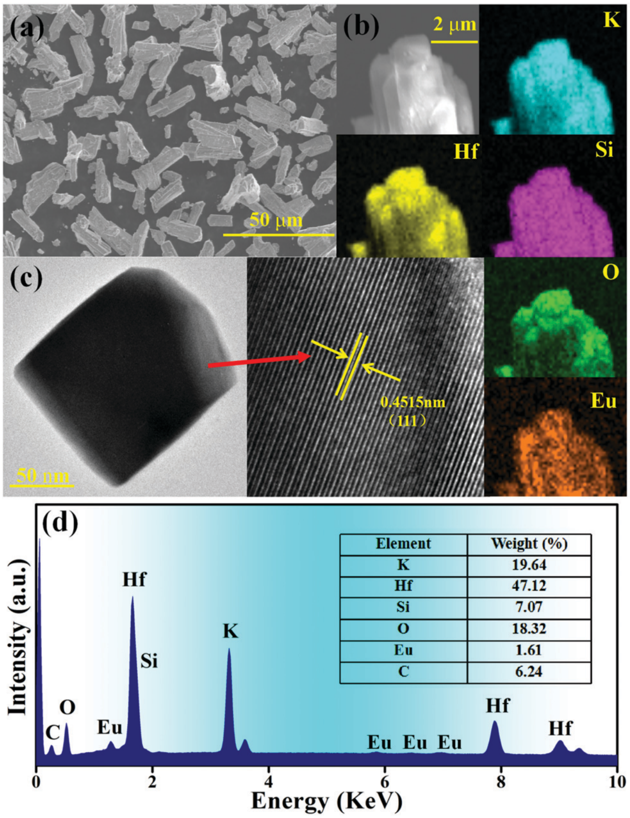

Fig. 2 (a) SEM image of K_2HfSiO_5:$0.02Eu^{2+}$; (b) SEM mapping (K, Hf, Si, O and Eu) of K_2HfSiO_5:$0.02Eu^{2+}$; (c) TEM and HTEM images of one K_2HfSiO_5:$0.02Eu^{2+}$ particle; and (d) EDX spectrum of K_2HfSiO_5:$0.02Eu^{2+}$.

The calculated band structure of K_2HfSiO_5 is shown in Fig. 3(a) and (b) according to the refined crystallographic results. It could be observed that K_2HfSiO_5 has an indirect band;[34] the maximum position of the valence band (VB) is located at point B and the minimum position of conduction band (CB) is located at point *G*. The calculated bandgap of K_2HfSiO_5 is 4.091 eV. The diffuse reflectance spectrum (DRS) of the K_2HfSiO_5 host displayed in Fig. 3(c) was taken to judge whether the calculation value is reliable. The optical bandgap of the K_2HfSiO_5 host could be obtained using the following formulae:

$$(\alpha h\nu)^{1/2} = A(h\nu - E_g) \tag{1}$$

$$\alpha = \frac{(1-R)^2}{2R} \tag{2}$$

In these equations, α refers to the absorption co-efficient, $h\nu$ is the incident photon energy, A is constant, and n = 1/2 corresponding to an indirect bandgap. As depicted in Fig. 3(c), the obtained optical bandgap of K_2HfSiO_5 is 4.125 eV. The value of the calculated bandgap is close to that of the optical bandgap, indicating the reliability of the calculation. This value illustrated that the $4f^65d \leftrightarrow 4f^7$ energy level transition of Eu^{2+} has little influence on the VB and CB of K_2HfSiO_5.[35]

Fig. 3(d) displays the calculated total Density of States (DOS) and partial Density of States (PDOS) of K_2HfSiO_5. The graph shows that the upper VB is mainly composed of the p-states of O element. The lower VB (−10 eV to −30 eV) involves the K s, p-states, Hf p-states, Si s, p-states and O s-states. These characteristics indicate the strong sp-hybridization of O-Hf and O-Si, which could be frequently seen in silicate inorganic hosts.[36] The CB is chiefly composed of K p-states. The DOS shows that the formation of the CB and VB includes the participation of all elements. All the above results show that K_2HfSiO_5 could be used as a potential host of luminescent materials.

Photoluminescence properties

Fig. 4(a) shows the PL spectra and PLE spectra of K_2HfSiO_5:$0.02Eu^{2+}$. When monitoring at 513 nm, a broad excitation band ranging from 250–480 nm has been detected, with a peak at 360 nm. Under 360 nm wavelength excitation, the K_2HfSiO_5:$0.02Eu^{2+}$ phosphor shows a cyan-green light

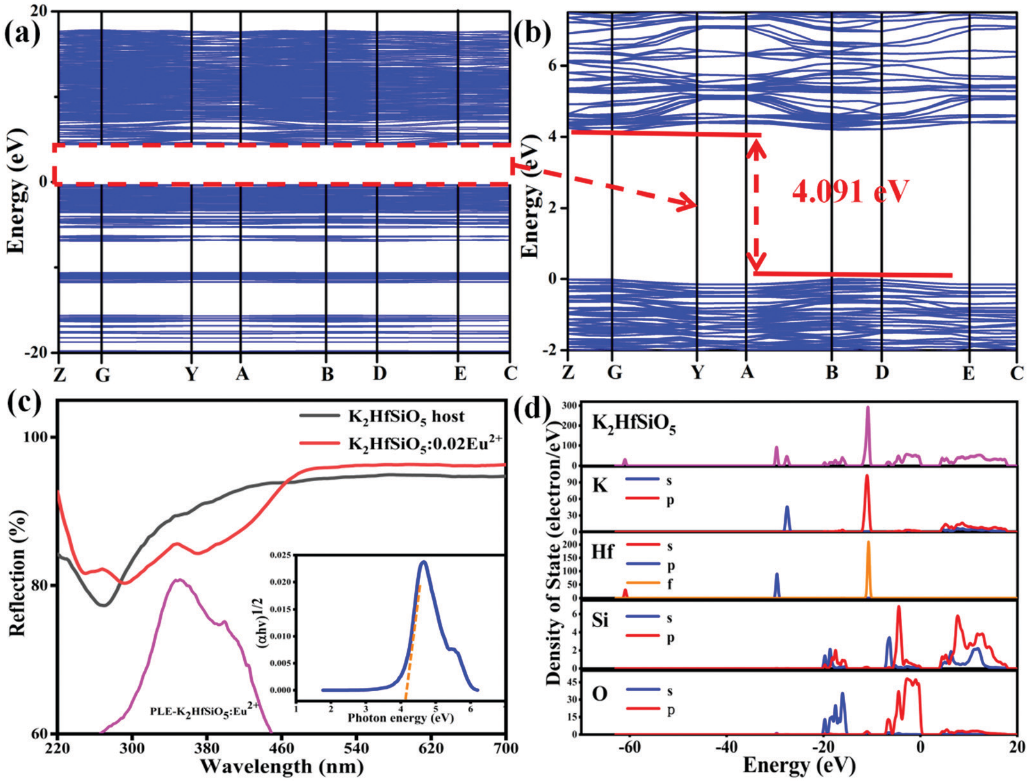

Fig. 3 (a) and (b) Band structure of K_2HfSiO_5; (c) the DRS spectra of Eu^{2+} doped and host of K_2HfSiO_5 (the inset shows the relationship between photon energy and $(\alpha h\nu)^{1/2}$ of the K_2HfSiO_5 host); (d) total and partial density of states of K_2HfSiO_5.

emission, exhibiting a wide emission band in the range of 400–650 nm with the maximum value located at 513 nm because of the 5d–4f energy transition of Eu^{2+}.[37,38] However, several sharp peaks appear in the range of 550–650 nm, which could be attributed to the energy transition of Eu^{3+}. In order to explore the reason of these peaks, the emission spectrum monitored at 394 nm is given in Fig. 4(b). It is found that the characteristic peak of Eu^{3+} was detected despite its intensity being weak. The sharp peaks at 570 nm, 586 nm, 598 nm, 615 nm and 650 nm correspond to the $^5D_0$–^7F_j (j = 0, 1, 2, 3 and 4) energy transition of Eu^{3+}, respectively. This result illustrates that a small amount of Eu^{3+} was not reduced to Eu^{2+} in K_2HfSiO_5:Eu^{2+}. Owing to the existence of Eu^{3+}, the K_2HfSiO_5:Eu phosphor is not suitable for light emitting diode (LED) devices. However, for the EDS layer, the characteristic emission of Eu^{3+} could increase the efficiency of the solar spectral conversion for solar cells.[39–41] The PL spectra of various concentrations of Eu^{2+} doped K_2HfSiO_5 are shown in Fig. 4(c). The optimum doping concentration is nearly about 2% with an internal quantum efficiency of 59.5% at this time. With the increase of Eu^{2+} concentration, the possibility of non-radiative energy transfer between Eu^{2+} was increasing, which would lead to concentration quenching.[42] The inset photo shows the time-resolved PL (TRPL) spectra of K_2HfSiO_5:0.02Eu^{2+}. It could be observed that the shape of TRPL spectra is consistent with that of PL spectra. Distinctly, different decay times have been detected when monitoring at the same wavelength, indicating that energy transfer occurs between different Eu^{2+} ions and further proving that there exist several luminescence centers in the K_2HfSiO_5:Eu^{2+} phosphor.[43]

There are three energy transfer methods among Eu^{2+} ions: radiation re-absorption, exchange interactions, or electric multipolar interactions.[42] It could be observed from Fig. 4(a) that the emission and excitation bands have a little overlap area, so that the effect of re-absorption is small. The parameter of critical distance (R_c) has been introduced to further confirm which mechanism of energy transfer between the different Eu^{2+} in K_2HfSiO_5:0.02Eu^{2+}. When $R_c \leq 5$ Å, the energy transfer mechanism is exchange interactions, otherwise it may be electric multipolar interactions. The value of R_c could be calculated using the following equation:[44]

$$R_C = 2\left(\frac{3V}{4\pi x_c Z}\right)^{1/3} \tag{3}$$

V is the volume of the unit cell, Z is the number of formula units and x_c is the optimal doping concentration. In the case of K_2HfSiO_5:Eu^{2+}, x_c = 0.02, Z = 8, and V = 975.51 Å^3. The calculated R_c is about 22.67 Å and this value is obviously larger than 5 Å, demonstrating that the electric multipolar interaction is the major energy transfer mechanism. The interaction type among Eu^{2+} activators could be analyzed

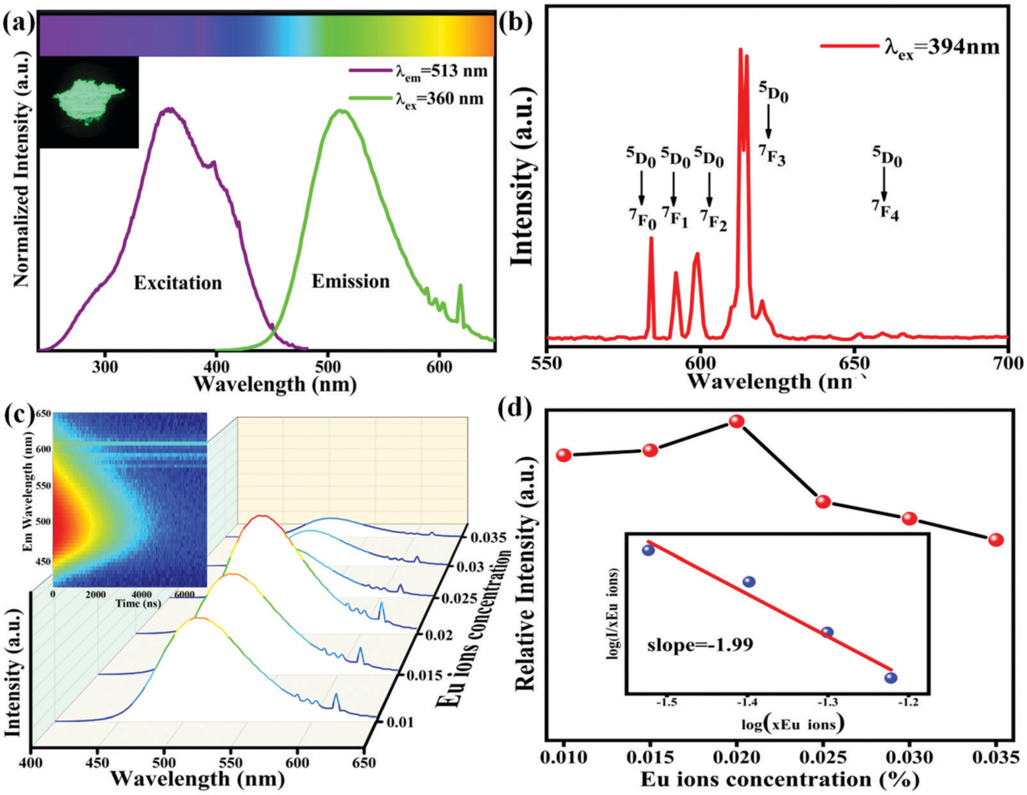

Fig. 4 (a) PLE and PL spectra of K_2HfSiO_5:$0.02Eu^{2+}$ (the inset shows the phosphor image under 365 nm ultraviolet light); (b) PL spectrum of K_2HfSiO_5:$0.02Eu^{2+}$ under 394 nm excitation; (c) the emission spectra of K_2HfSiO_5:xEu^{2+} ($0.01 \le x \le 0.35$) (the inset represents the TRPL spectra); and (d) the relative emission intensity of K_2HfSiO_5:xEu^{2+} ($0.01 \le x \le 0.35$) samples (the inset shows the curve of log(x) and log(I/x).).

by Dexter's theory using the following formula:[45]

$$\frac{I}{x} = \frac{k}{1+\beta(x)^{\frac{\theta}{3}}} \tag{4}$$

The factor x refers to the doping concentration of Eu^{2+}, θ = 6, 8 or 10 representing the dipole–dipole, dipole–quadrupole and quadrupole–quadrupole interactions, respectively. What's more, k and β are constants. Fig. 4(d) inset shows the fitting line of log (x) and log (I/x). The slope of this line represents $\theta/3$. For K_2HfSiO_5:xEu^{2+} ($0.01 \le x \le 0.035$) samples, the calculated result of θ is close to 6, demonstrating that the energy transfer interaction type of K_2HfSiO_5:Eu^{2+} is dipole–dipole.

To further probe the reason for the concentration quenching of the K_2HfSiO_5:Eu^{2+} phosphor, Fig. 5 depicts the decay curves of the K_2HfSiO_5:xEu^{2+} ($0.01 \le x \le 0.035$) samples and all the decay curves could be fitted by the following formula[30]:

$$I(t) = A_1\exp\left(-\frac{t}{\tau_1}\right) + A_2\exp\left(-\frac{t}{\tau_2}\right) + A_3\exp\left(-\frac{t}{\tau_3}\right) \tag{5}$$

where A_1, A_2 and A_3 are constants, I is the emission intensity, t is the time and τ_1, τ_2 and τ_3 are the lifetimes. The average decay time of every sample could be obtained using the formula as follows:

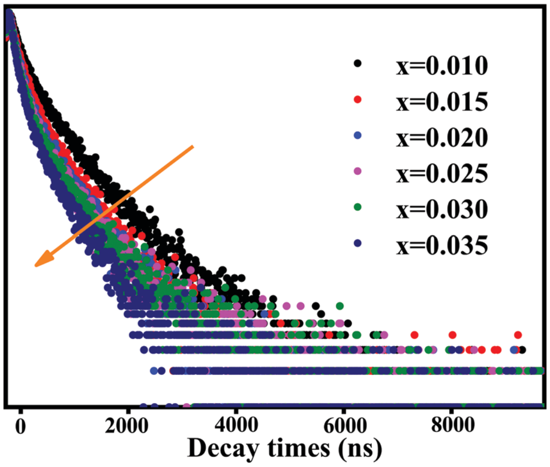

Fig. 5 The decay curves of the K_2HfSiO_5:xEu^{2+} ($0.01 \le x \le 0.035$) samples.

$$\tau = \frac{A_1{\tau_1}^2 + A_2{\tau_2}^2 + A_3{\tau_3}^2}{A_1\tau_1 + A_2\tau_2 + A_3\tau_3} \tag{6}$$

According to this formula, the average decay times of different concentrations of Eu^{2+} doping samples are 512, 505, 486, 478, 468 and 455 ns, separately. With the increase of Eu^{2+}, the decay time of K_2HfSiO_5:Eu^{2+} keeps decreasing. This could

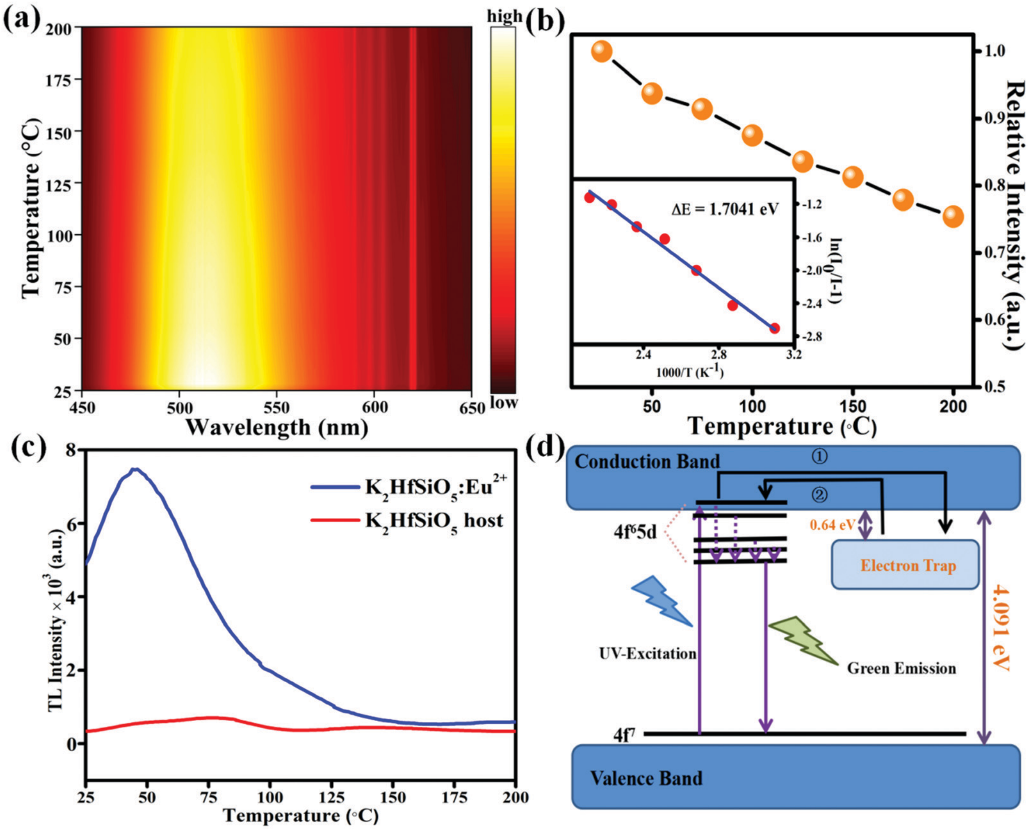

Fig. 6 (a) Temperature dependent luminescence spectra of K_2HfSiO_5:$0.02Eu^{2+}$ phosphor from 25 to 200 °C; (b) the relative emission intensity of K_2HfSiO_5:$0.02Eu^{2+}$ at different temperatures (the inset shows the fitting activation energy of K_2HfSiO_5:$0.02Eu^{2+}$); (c) the thermoluminescence (TL) curves of K_2HfSiO_5:$0.02Eu^{2+}$ and K_2HfSiO_5 host; and (d) the energy level diagram of Eu^{2+} in K_2HfSiO_5.

be ascribed to the fact that the distance between the activators becomes shorter with the increase of the Eu^{2+} doping amount. Therefore, non-radiative energy transfer is more likely to occur in K_2HfSiO_5:Eu^{2+}, leading to concentration quenching of Eu^{2+}.[46]

The thermal stability of K_2HfSiO_5:Eu^{2+} is shown in Fig. 6(a). It could be found that the emission intensity decreased with the temperature increase from 25 °C to 200 °C; the position of emission almost doesn't shift. Fig. 6(b) shows the relative emission intensity with a linear increase in temperature. When it reached 150 °C, K_2HfSiO_5:$0.02Eu^{2+}$ could still retain about 81.2% of its initial emission intensity. This result shows that the thermal stability of K_2HfSiO_5:Eu^{2+} is apparently higher than that of Na_2HfSiO_5:Eu^{2+} (retains 45% at 150 °C) and K_2ZrSiO_5:Eu^{2+} (retains 19.4% at 150 °C) phosphors. To understand the reason why the K_2HfSiO_5:Eu^{2+} phosphor has great thermal stability, the activation energy (ΔE) could be calculated according to the Arrhenius equation:[47]

$$I_T = \frac{I_0}{1 + c\exp\left(-\frac{\Delta E}{kT}\right)} \tag{7}$$

where I_0 is the emission intensity at initial temperature, I_T represents the intensity at heating temperature, c and k are constant, and ΔE is the activation energy. As shown in the inset of Fig. 6(b), the calculated value of ΔE of K_2HfSiO_5:$0.02Eu^{2+}$ is 1.7041 eV. The larger value of the activation energy might be one of the reasons for the excellent thermal stability of the K_2HfSiO_5:$0.02Eu^{2+}$ phosphor.

The thermoluminescence curves of the K_2HfSiO_5 host and K_2HfSiO_5:Eu^{2+} are shown in Fig. 6(c). It could be obviously seen that there exists an electron trap at about at 50 °C in K_2HfSiO_5:Eu^{2+}. The trap depth could be estimated using the following formula:

$$E_T = \frac{T_m}{500} \tag{8}$$

E_T refers to the depth of the energy trap, and T_m is the position of the TL peak. The calculated trap depth is about 0.64 eV at 50 °C. Based on the above result, the simulated energy level schematic diagram of Eu^{2+} in K_2HfSiO_5 is plotted in Fig. 6(d). The electron trap is considered to be close to the bottom of the conduction band. The electrons will be excited from the $4f^7$ ground state to the 5d state with 360 nm excitation. Some of the electrons could directly transit back to the ground state level, resulting in green emission, while other electrons in a higher excited state level could be trapped through the conduction band (procedure ①). Subsequently, as the temperature increases, the trapped electrons are released through the conduction band (procedure ②). The electrons return to the excited state and come to the ground state, leading to an increase of the emission intensity.[48] This is another reason for $K_2HfSiO_5:Eu^{2+}$ possessing great thermal stability.

Cathodoluminescence properties

The cathodoluminescence (CL) performance is vital for the display of radar, television and oscilloscope.[49–51] Fig. 7(a) and (b) show the SEM and CL mapping images of one $K_2HfSiO_5:0.02Eu^{2+}$ particle. These graphs demonstrate that luminescence centers are distributed on the particle evenly.

Fig. 7(c) represents the CL spectra of $K_2HfSiO_5:0.02Eu^{2+}$ under increasing voltage. The shape of the CL spectra is similar to the PL spectra which are shown in Fig. 4(a). When the current remains at 60 mA, the CL intensity of $K_2HfSiO_5:0.02Eu^{2+}$ continuously increases with the growing voltage (5–10 kV). This phenomenon could be explained by the electron penetration depth and the value could be calculated using the following formula:[52]

$$L(\text{Å}) = 250\left(\frac{A}{\rho}\right)\left(\frac{E}{\sqrt{Z}}\right)^n,\ n = \frac{1.2}{1 - 0.29lgZ} \qquad (9)$$

In this case, A is the molecular weight of K_2HfSiO_5, Z indicates the atomic number, ρ refers to the density, and E is the loading voltage (kV). For $K_2HfSiO_5:Eu^{2+}$, $A = 364.77$, $Z = 207$ and $\rho = 4.97$ g cm^{-3}. The calculated electron penetration depths are 25.45 (6 kV), 92.31 (8 kV) and 307.69 (10 kV) nm, respectively. Moreover, as shown in Fig. 7(d), the CL intensity also increases with different currents varying from 50–100 mA. The deeper the electron penetration depth, the more luminescence centers detected, leading to an increase of the CL intensity.

The anti-degradation properties of $K_2HfSiO_5:0.02Eu^{2+}$ have been tested under certain conditions (6 kV, 60 mA) shown in Fig. 8. Obviously, the CL intensity decreases slowly with the electron bombardment from 10 to 90 min. It is well known that graphite carbon will accumulate in the process of high current density electron beam irradiation. This accumulation will not only prevent low-energy electrons from reaching the phosphor particles, but also aggravate surface charging which leads to the decrease of CL intensity.[53] It can be observed from Fig. 8 that the CL intensity still remains about 80.12% of the initial intensity, indicating that the CL stability of $K_2HfSiO_5:0.02Eu^{2+}$ is perfect. Meanwhile, the color stability and peak position of $K_2HfSiO_5:0.02Eu^{2+}$ are almost unchanged. All the above results demonstrate that the $K_2HfSiO_5:Eu^{2+}$ phosphor possesses outstanding CL properties and has potential application in CL devices.

Applications

Energy-down-shift layer for $CsPbI_3$ solar cells. The $K_2HfSiO_5:Eu^{2+}$ phosphor was used to fabricate an energy-down-shift (EDS) layer for $CsPbI_3$ solar cells.[6,54–56] The morphology and particle size of $K_2HfSiO_5:0.02Eu^{2+}$ phosphor are displayed in Fig. 9(a) and (b). In order to make the EDS layer have a better effect, the particle size was further reduced to an average value of 2.51 μm. Fig. 9(c) exhibits the feasibility of

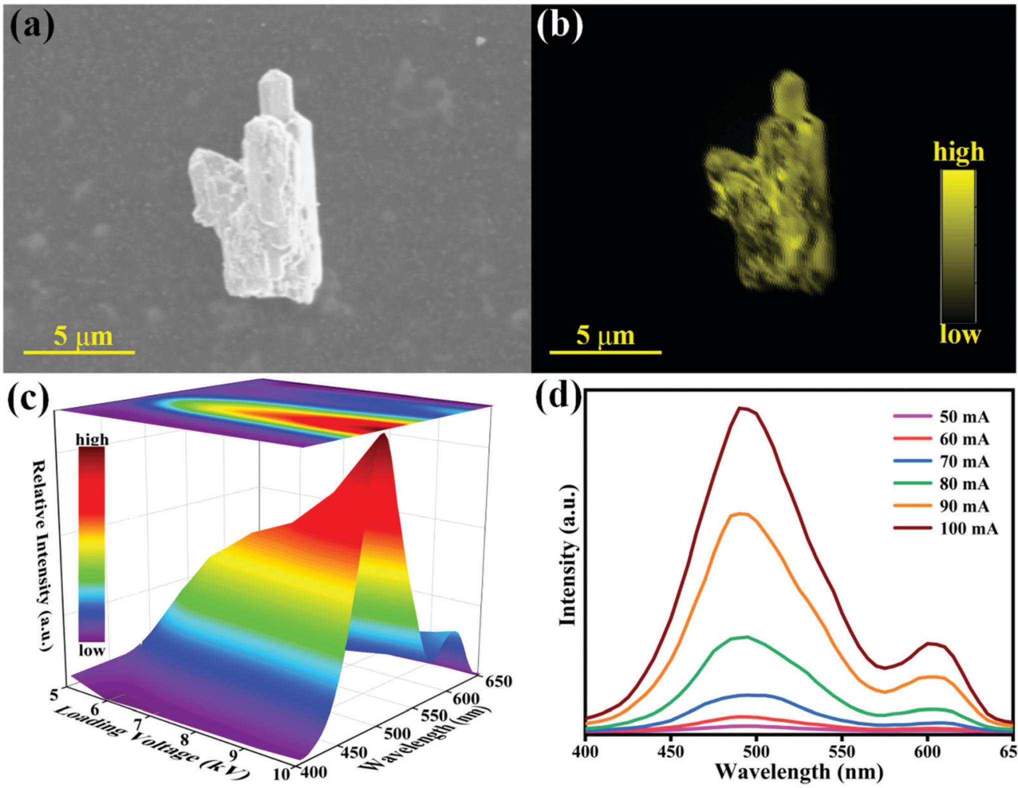

Fig. 7 The SEM image (a) and CL mapping (b) of one $K_2HfSiO_5:0.02Eu^{2+}$ particle; (c) the CL intensity of $K_2HfSiO_5:0.02Eu^{2+}$ with various voltage (4–9 kV); and (d) the CL spectra of $K_2HfSiO_5:0.02Eu^{2+}$ with different current (50–100 mA).

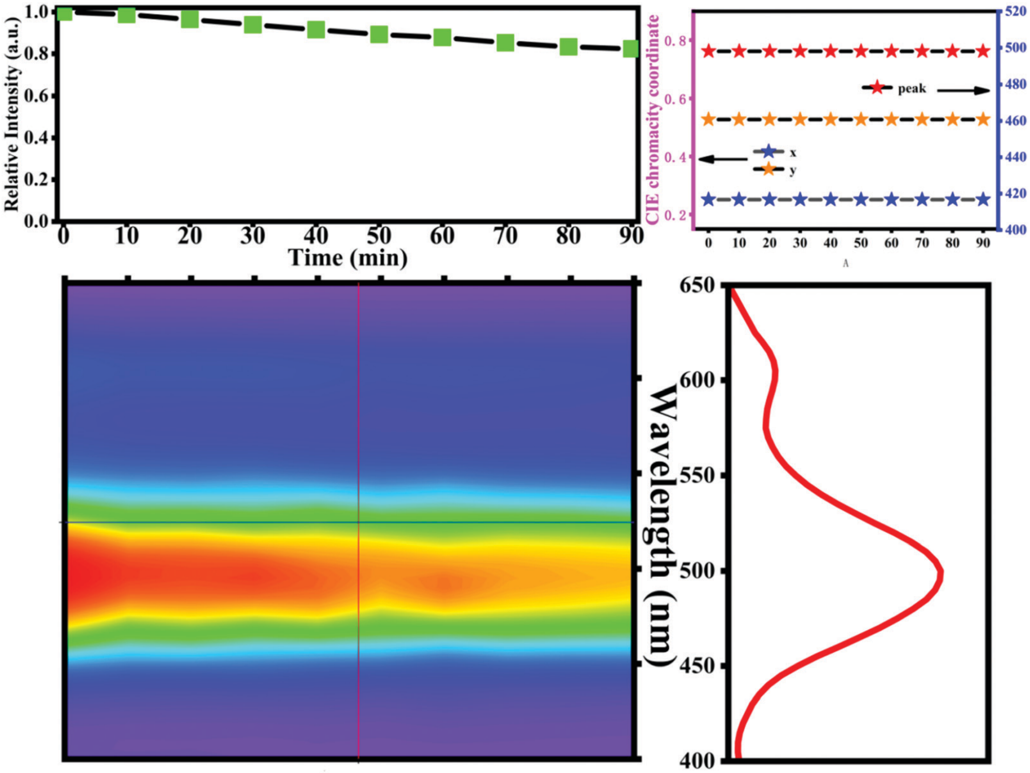

Fig. 8 The anti-degradation properties and the relative intensity of K_2HfSiO_5:0.02Eu^{2+} under sustained electron bombardment (the top right corner represents the change of CIE coordinates and peak position).

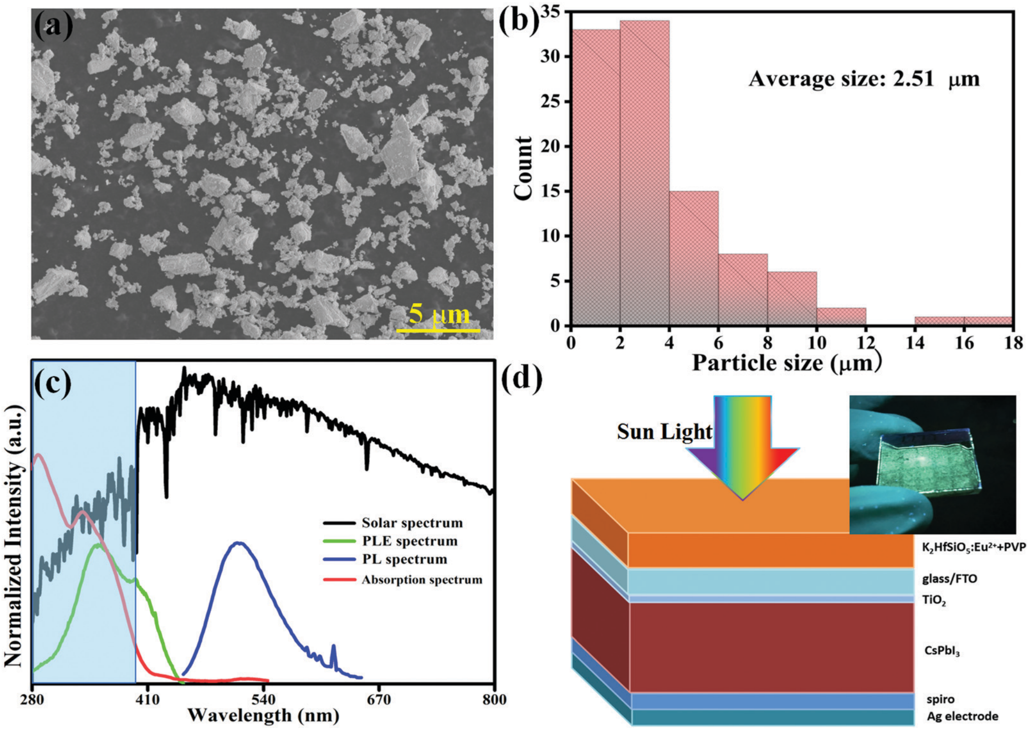

Fig. 9 (a) The SEM image of K_2HfSiO_5:0.02Eu^{2+} particles for the energy-down-shift layer; (b) the average size of K_2HfSiO_5:0.02Eu^{2+} phosphor; (c) solar spectrum, emission spectrum of K_2HfSiO_5:0.02Eu^{2+} under 360 nm excitation, excitation spectrum monitored at 513 nm and the absorption spectrum of coated solar cell; and (d) schematic structure of $CsPbI_3$ solar cells coated with the EDS layer.

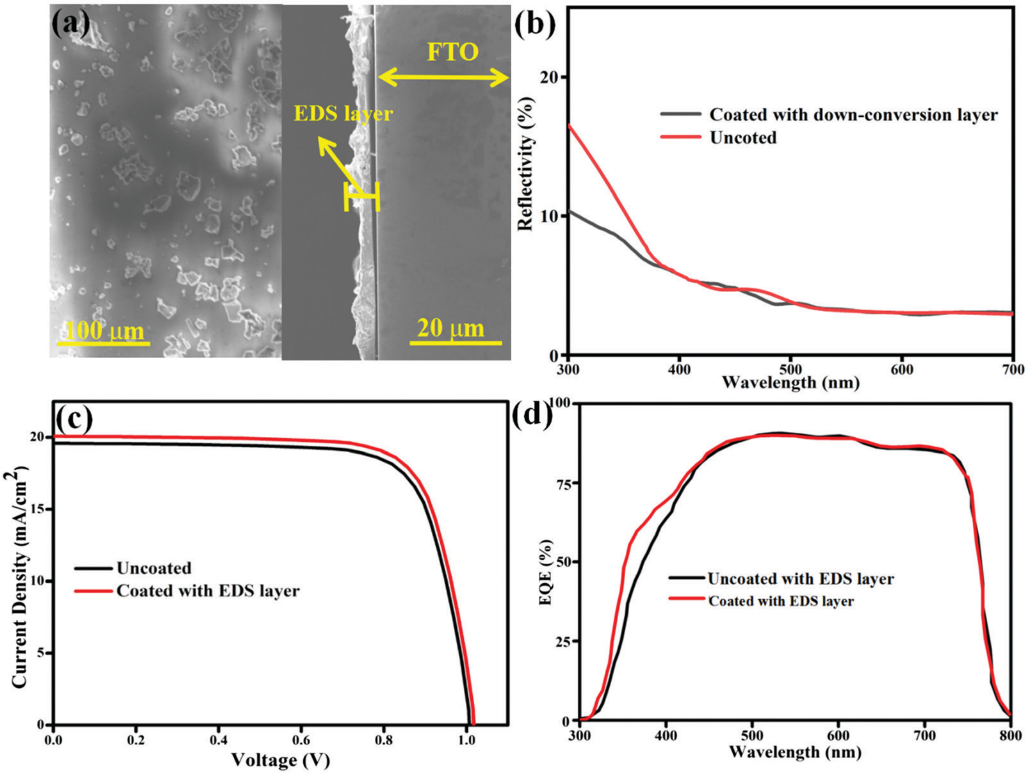

Fig. 10 (a) SEM images of the EDS layer in vertical and side views; (b) reflection spectra of solar cells; (c) *I*–*V* curves of solar cells; (d) the EQE spectra of $CsPbI_3$ solar cells with coated and uncoated solar cells.

making the EDS layer using the K_2HfSiO_5:Eu^{2+} phosphor. The overlap of the excitation spectrum (green curve) and the strong absorption spectrum of solar cell device (red curve) illustrate that the K_2HfSiO_5:Eu^{2+} EDS layer has the ability to make the UV light from the sun light be effectively absorbed by $CsPbI_3$ solar cells due to the down-conversion effect.[57] The $CsPbI_3$ solar cells coated with the EDS layer have been packaged as shown in the schematic diagram in Fig. 9(d) according to the above analysis. The structure of the packaged $CsPbI_3$ solar cells with the K_2HfSiO_5:Eu^{2+} EDS layer is K_2HfSiO_5:Eu^{2+} EDS layer/FTO/TiO_2/$CsPbI_3$ film/spiro-OMeTAD/electrode. After packaging the spin-coated solar cells according to the schematic diagram and putting it under the irradiation of a 365 nm ultraviolet-lamp, they presented a cyan-green light as shown in the inset of Fig. 9(d), which is consistent with the emission color of K_2HfSiO_5:$0.02Eu^{2+}$ phosphor.

In order to more intuitively illustrate the successful application of the EDS layer on $CsPbI_3$ solar cells, the EDS layer was spin coated on FTO and characterized by SEM as shown in Fig. 10(a). According to the vertical view, the K_2HfSiO_5:Eu^{2+} phosphor in the EDS layer is evenly distributed in the film-forming agent PVP, and there is no obvious agglomeration of phosphor particles. The side view clearly shows that the EDS layer is a film with an average thickness of nearly about 2 μm. It could be seen from the reflection spectra in Fig. 10(b) that the reflectivity of the solar cells coated with the EDS layer has decreased. Therefore, it can be concluded that part of the UV light has been converted into visible light. The *I*–*V* curves are measured as shown in Fig. 10(c). When coated with this EDS layer, the J_{SC} shows an increasing tendency after coated with the EDS layer. To further verify the effect of the K_2HfSiO_5:Eu^{2+} phosphor EDS layer, the external quantum efficiency (EQE) spectra are shown in Fig. 10(d). In the range of UV light, the value of uncoated sample is lower than that of the coated sample. However, the EQE curves of the two samples are similar in other ranges of light. Therefore, it can be concluded that the increase of J_{sc} is related to the application of the energy transfer layer. PCE could be calculated from the parameters shown in Table 4:

This result shows that the $CsPbI_3$ solar cells coated with the EDS layer present a higher PCE value of 16.83%, with an amplification of 2.19% compared with that of the bare cell. These results indicate that K_2HfSiO_5:$0.02Eu^{2+}$ could be used as an EDS layer to improve the PCE of $CSPbI_3$ solar cells. At the same time, it also provides the possibility for the combination of the luminescence material and perovskite solar cell technology.

Table 4 Key *I*-*V* parameters of $CsPbI_3$ solar cells coated with and without the EDS layer

Sample	V_{oc} (V)	J_{SC} (mA cm^{-2})	Fill factor (%)	PCE (%)	ΔPCE (%)
Bare cell	1.007	19.77	72.47	16.35	2.19
Coated cell	1.012	20.05	72.48	16.73	

4. Conclusions

In this work, a series of K_2HfSiO_5:$x$$Eu^{2+}$ ($0.01 \leq x \leq 0.035$) phosphors were successfully designed and synthesized for the first time. The structure, morphology and bandgap were investigated in detail. Under 360 nm excitation, the K_2HfSiO_5:0.02Eu^{2+} phosphor emits a high efficiency cyan-green light and the peak is located at 513 nm. After the feasibility analysis, we packaged the $CsPbI_3$ solar cells coated with the K_2HfSiO_5:0.02Eu^{2+} phosphor EDS layer and the major electrochemical parameters were increased. Under the sustained electron-beam excitation, the K_2HfSiO_5:0.02Eu^{2+} phosphor shows excellent anti-degradation properties and a perfect color stability. In addition, since the K_2HfSiO_5:Eu^{2+} phosphor has potential for multifunctional application, we can imagine that in future, we can use the K_2HfSiO_5:Eu^{2+} EDS layer to improve the photoelectric conversion rate of solar cells, and then apply the electric energy to cathodoluminescence devices fabricated using the K_2HfSiO_5:Eu^{2+} phosphor. All the above results offer us a novel way to achieve effective utilization of solar energy.

Conflicts of interest

There are no conflicts to declare.

References

1 M. Ali, R. Riaz, S. Bae, H.-S. Lee, S. H. Jeong and M. J. Ko, Layer-by-Layer self-assembly of hollow nitrogen-doped carbon quantum dots on cationized textured crystalline silicon solar cells for an efficient energy down-shift, *ACS Appl. Mater. Interfaces*, 2020, **12**, 10369–10381.

2 R. Riaz, M. Ali, T. Maiyalagan, A. S. Anjum, S. Lee, M. J. Ko and S. H. Jeong, Dye-sensitized solar cell (DSSC) coated with energy down shift layer of nitrogen-doped carbon quantum dots (N-CQDs) for enhanced current density and stability, *Appl. Surf. Sci.*, 2019, **483**, 425–431.

3 B. Ren and C. Jiang, Designing a multi-quantum-dot-doped wavelength down-shifting model of c-Si solar cells by using machine learning, *Appl. Opt.*, 2020, **59**, 985–990.

4 J. M. Ball, S. D. Stranks, M. T. Hörantner, S. Hüttner, W. Zhang, E. J. Crossland, I. Ramirez, M. Riede, M. B. Johnston and R. H. Friend, Optical properties and limiting photocurrent of thin-film perovskite solar cells, *Energy Environ. Sci.*, 2015, **8**, 602–609.

5 H. Bian, Q. Wang, S. Yang, C. Yan, H. Wang, L. Liang, Z. Jin, G. Wang and S. F. Liu, Nitrogen-doped graphene quantum dots for 80% photoluminescence quantum yield for inorganic γ-$CsPbI_3$ perovskite solar cells with efficiency beyond 16%, *J. Mater. Chem. A*, 2019, **7**, 5740–5747.

6 M. Jalalah, Y.-H. Ko, F. A. Harraz, M. Al-Assiri and J.-G. Park, Enhanced efficiency and current density of solar cells via energy-down-shift having energy-tuning-effect of highly UV-light-harvesting Mn^{2+}-doped quantum dots, *Nano Energy*, 2017, **33**, 257–265.

7 X. Zhang, H. Huang, X. Ling, J. Sun, X. Jiang, Y. Wang, D. Xue, L. Huang, L. Chi, J. Yuan and W. Ma, Homojunction Perovskite Quantum Dot Solar Cells with over 1 μm-Thick Photoactive Layer, *Adv. Mater.*, 2021, **33**, 2105977.

8 J. Yuan, X. Zhang, J. Sun, R. Patterson, H. Yao, D. Xue, Y. Wang, K. Ji, L. Hu, S. Huang, D. Chu, T. Wu, J. Hou and J. Yuan, Hybrid Perovskite Quantum Dot/Non-Fullerene Molecule Solar Cells with Efficiency Over 15%, *Adv. Funct. Mater.*, 2021, 2101272.

9 J. Yuan, N. Rujisamphan, W. Ma, J. Yuan, Y. Li and S. T. Lee, Perspective on the perovskite quantum dots for flexible photovoltaics, *J. Energy Chem.*, 2021, **62**, 505–507.

10 Z. Li, J. Guo, Z. Li, W. Han, G. Ren, C. Liu, L. Shen and W. Guo, Incorporating self-assembled silane-crosslinked carbon dots into perovskite solar cells to improve efficiency and stability, *J. Mater. Chem. A*, 2020, **8**, 5629–5637.

11 L. Liang, M. Liu, Z. Jin, Q. Wang, H. Wang, H. Bian, F. Shi and S. Liu, Optical management with nanoparticles for a light conversion efficiency enhancement in inorganic γ-$CsPbI_3$ solar cells, *Nano Lett.*, 2019, **19**, 1796–1804.

12 P. V. Kamat, *Emergence of new materials for light–energy conversion: perovskites, metal Clusters, and 2-D Hybrids*, ACS Publications, 2014.

13 S. C. Liu, Y. Yang, Z. Li, D. J. Xue and J. S. Hu., GeSe thin-film solar cells, *Mater. Chem. Front.*, 2020, **4**(3), 775–787.

14 W. T. Li, Q. S. Liu, K. Jin, M. Cheng, F. Hao, W. Q. Wu, S. J. Liu, Z. Xiao, S. F. Yang, A. W. Shi and L. M. Ding, Fused-ring phenazine building blocks for efficient copolymer donors, *Mater. Chem. Front.*, 2020, 1454–1458.

15 P. Pust, P. J. Schmidt and W. Schnick, A revolution in lighting, *Nat. Mater.*, 2015, **14**, 454–458.

16 H. A. Höppe, Recent developments in the field of inorganic phosphors, *Angew. Chem., Int. Ed.*, 2009, **48**, 3572–3582.

17 B. S. Richards, Luminescent layers for enhanced silicon solar cell performance: Down-conversion, *Sol. Energy Mater. Sol. Cells*, 2006, **90**, 1189–1207.

18 P. Du, J. Ma, Q. Zhu and J. G. Li, Phase evolution, structure, and up-/down-conversion luminescence of $Li_6CaLa_2Nb_2O_{12}$: Yb^{3+}/RE^{3+} phosphors (RE = Ho, Er, Tm), *J. Am. Ceram. Soc.*, 2020, **103**, 2674–2685.

19 L. Gao, Y. Yan, Y. Li and T. Ma, Comparison of Physical Isolation on Large Active Area Perovskite Solar Cells, *Chem. Res. Chin. Univ.*, 2020, **36**, 1279–1283.

20 X. Qin, X. Liu, W. Huang, M. Bettinelli and X. Liu, Lanthanide-activated phosphors based on 4f-5d optical transitions: theoretical and experimental aspects, *Chem. Rev.*, 2017, **117**, 4488–4527.

21 Z. Hosseini, E. W. G. Diau, K. Mehrany and N. Taghavinia, Assessment of Luminescent Downshifting Layers for the Improvement of Light-Harvesting Efficiency in Dye-Sensitized Solar Cells, *ChemPhysChem*, 2014, **15**, 3791–3799.

22 Y.-C. Fang, P.-C. Kao, Y.-C. Yang and S.-Y. Chu, Two-step synthesis of $SrSi_2O_2N_2$: Eu^{2+} green oxynitride phosphor: electron-phonon coupling and thermal quenching behavior, *J. Electrochem. Soc.*, 2011, **158**, J246.

23 J. Wang, H. Zhang, B. Lei, H. Dong, H. Zhang, Y. Liu, M. Zheng and Y. Xiao, Optical energy storage properties of $(Ca_{1-x}Sr_x)_2Si_5N_8$: Eu^{2+},Tm^{3+} solid solutions, *J. Am. Ceram. Soc.*, 2015, **98**, 1823–1828.

24 Z. Xia, Y. Zhang, M. S. Molokeev and V. V. Atuchin, Structural and luminescence properties of yellow-emitting $NaScSi_2O_6$: Eu^{2+} phosphors: Eu^{2+} site preference analysis and generation of red emission by codoping Mn^{2+} for white-light-emitting diode applications, The, *J. Phys. Chem. C*, 2013, **117**, 20847–20854.

25 H. Liao, M. Zhao, M. S. Molokeev, Q. Liu and Z. Xia, Learning from a mineral structure toward an ultra-narrow-band blue-emitting silicate phosphor $RbNa_3$ $(Li_3SiO_4)_4$: Eu^{2+}, *Angew. Chem.*, 2018, **130**, 11902–11905.

26 J. K. Park, C. H. Kim, S. H. Park, H. D. Park and S. Y. Choi, Application of strontium silicate yellow phosphor for white light-emitting diodes, *Appl. Phys. Lett.*, 2004, **84**, 1647–1649.

27 X. Xu, Q. Shao, L. Yao, Y. Dong and J. Jiang, Highly efficient and thermally stable Cr^{3+} -activated silicate phosphors for broadband near-infrared LED applications, *Chem. Eng. J.*, 2020, **383**, 123108.

28 X. Tong, J. Han, R. Cai, Y. Xu, P. Wu, H. Zhou and X. Zhang, Multisite-occupancy-driven efficient multiple energy transfer: a straightforward strategy to achieve single-composition white-light emission in Ce^{3+}-, Tb^{3+}-, and Mn^{2+}-doped silicate phosphors, *Inorg. Chem.*, 2020, **59**, 9838–9846.

29 R. Nagaraj, A. Raja and S. Ranjith, Synthesis and luminescence properties of novel red-emitting Eu^{3+} ions doped silicate phosphors for photonic applications, *J. Alloys Compd.*, 2020, **827**, 154289.

30 Q. Wu, J. Ding and J. Zhou, Insight into a Eu^{2+}-activated zirconium-silicate yellow phosphor for multifunctional applications, *Ceram. Int.*, 2020, **46**, 20545–20552.

31 B. H. Toby, EXPGUI, a graphical user interface for GSAS, *J. Appl. Crystallogr.*, 2001, **34**, 210–213.

32 M. Segall, P. J. Lindan, M.a. Probert, C. J. Pickard, P. J. Hasnip, S. Clark and M. Payne, First-principles simulation: ideas, illustrations and the CASTEP code, *J. Phys.: Condens. Matter*, 2002, **14**, 2717.

33 O. Eritsyan, Diffraction reflection of light in a cholesteric liquid crystal in the presence of wave irreversibility and Bragg formula for media with nonidentical forward and return wavelengths, *J. Exp. Theor. Phys.*, 2000, **90**, 102–108.

34 G. Cassabois, P. Valvin and B. Gil, Hexagonal boron nitride is an indirect bandgap semiconductor, *Nat. Photonics*, 2016, **10**, 262–266.

35 Q. Wei, J. Ding and Y. Wang, A novel wide-excitation and narrow-band blue-emitting phosphor with hafnium silicon multiple rings structure for photoluminescence and cathodoluminescence, *J. Alloys Compd.*, 2020, **831**, 154825.

36 D. Magero, M. E. Casida, G. Amolo, N. Makau and L. Kituyi, Partial density of states ligand field theory (PDOS-LFT): Recovering a LFT-like picture and application to photoproperties of ruthenium(II) polypyridine complexes, *J. Photochem. Photobiol., A*, 2017, **348**, 305–325.

37 P. Dorenbos, Energy of the first 4f7 → 4f65d transition of Eu^{2+} in inorganic compounds, *J. Lumin.*, 2003, **104**, 239–260.

38 E. Elzer, P. Strobel, V. Weiler, P. J. Schmidt and W. Schnick, Illuminating nitridoberylloaluminates: the highly efficient red-emitting phosphor Sr_2 $[BeAl_3N_5]$: Eu^{2+}, *Chem. Mater.*, 2020, **32**, 6611–6617.

39 X. Yang, J. Chen, S. Zheng and C. Chen, A downshifting Eu^{3+} doped glass embedded with concave pyramid microstructure to improve the efficiency of silicon solar cell, *J. Rare Earths*, 2020, **38**, 1158–1164.

40 K. Jha and M. Jayasimhadri, Effective sensitization of Eu^{3+} and energy transfer in Sm^{3+}/Eu^{3+} co-doped ZPBT glasses for CuPc based solar cell and w-LED applications, *J. Lumin.*, 2018, **194**, 102–107.

41 J. Garcia, L. Bontempo, L. Gomez-Malagon and L. Kassab, Efficiency boost in Si-based solar cells using tellurite glass cover layer doped with Eu^{3+} and silver nanoparticles, *Opt. Mater.*, 2019, **88**, 155–160.

42 D. L. Dexter and J. H. Schulman, Theory of concentration quenching in inorganic phosphors, *J. Chem. Phys.*, 1954, **22**, 1063–1070.

43 R. Shi, L. Ning, Z. Wang, J. Chen, T. K. Sham, Y. Huang, Z. Qi, C. Li, Q. Tang and H. Liang, Zero-thermal quenching of Mn^{2+} red luminescence via efficient energy transfer from Eu^{2+} in $BaMgP_2O_7$, *Adv. Opt. Mater.*, 2019, **7**, 1901187.

44 G. Blasse, Energy transfer in oxidic phosphors, *Phys. Lett. A*, 1968, **28**, 444–445.

45 D. L. Dexter, A theory of sensitized luminescence in solids, *J. Chem. Phys.*, 1953, **21**, 836–850.

46 N. J. Johnson, S. He, S. Diao, E. M. Chan, H. Dai and A. Almutairi, Direct evidence for coupled surface and concentration quenching dynamics in lanthanide-doped nanocrystals, *J. Am. Chem. Soc.*, 2017, **139**, 3275–3282.

47 K. Shioi, N. Hirosaki, R.-J. Xie, T. Takeda and Y. Q. Li, Photoluminescence and thermal stability of yellow-emitting Sr-α-SiAlON: Eu^{2+} phosphor, *J. Mater. Sci.*, 2010, **45**, 3198–3203.

48 Q. Wei, J. Ding and Y. Wang, A novel tunable extra-broad yellow-emitting nitride phosphor with zero-thermal-quenching property, *Chem. Eng. J.*, 2020, **386**, 124004.

49 J. Götze and U. Kempe, A comparison of optical microscope- and scanning electron microscope-based cathodoluminescence (CL) imaging and spectroscopy applied to geosciences, *Mineral. Mag.*, 2008, **72**, 909–924.

50 S. Meuret, Y. Auad, L. Tizei, H. Chang, F. Houdellier, M. Kociak and A. Arbouet, Time-resolved Cathodoluminescence in a Transmission Electron Microscope Applied to NV Centers in Diamond, *Microsc. Microanal.*, 2020, **26**, 2022–2023.

51 F. Ammari, N. Del-Solar-Velarde, R. Chapoulie and B. Bousquet, Chemometrics applied to cathodoluminescence images: a new approach to classify pre-Columbian artefacts from northern Peru, *Environ. Sci. Pollut. Res.*, 2017, **24**, 2205–2209.

52 G. Li, C. Li, C. Zhang, Z. Cheng, Z. Quan, C. Peng and J. Lin, Tm^{3+} and/or Dy^{3+} doped LaOCl nanocrystalline phosphors for field emission displays, *J. Mater. Chem.*, 2009, **19**, 8936–8943.

53 P. Wen, S. Zhang, D. Li, J. Liu, L. Zhang, K. Zhou, M. Feng, A. Tian, F. Zhang and X. Gao, Identification of degradation mechanisms of blue InGaN/GaN laser diodes, *J. Phys. D: Appl. Phys.*, 2015, **48**, 415101.

54 Q. Wang, X. Zhang, Z. Jin, J. Zhang, Z. Gao, Y. Li and S. F. Liu, Energy-down-shift $CsPbCl_3$: Mn quantum dots for boosting the efficiency and stability of perovskite solar cells, *ACS Energy Lett.*, 2017, **2**, 1479–1486.

55 J. Jin, H. Li, W. Bi, C. Chen, B. Zhang, L. Xu, B. Dong, H. Song and Q. Dai, Efficient and stable perovskite solar cells through e-beam preparation of cerium doped TiO_2 electron transport layer, ultraviolet conversion layer $CsPbBr_3$ and the encapsulation layer Al_2O_3, *Sol. Energy*, 2020, **198**, 187–193.

56 Ç. Kırbıyık, A. Toprak, C. Başlak, M. Kuş and M. Ersöz, Nitrogen-doped CQDs to enhance the power conversion efficiency of perovskite solar cells via surface passivation, *J. Alloys Compd.*, 2020, **832**, 154897.

57 Y. Wang, Y. Chang, J. Zhang, G. Lu and Z. Wei, Semitransparent Flexible Organic Solar Cells, *Chem. Res. Chin. Univ.*, 2020, **36**, 343–350.